Mathematics

Case report

A time-stepping BEM for three-dimensional thermoelastic fracture problems of anisotropic functionally graded materials

Mohamed Abdelsabour Fahmy[1,*] and Ahmad Almutlg[2]

[1] Department of Mathematics, Adham University College, Umm Al-Qura University, Adham 28653, Makkah, Saudi Arabia

[2] Department of Mathematics, College of Science, Qassim University, Buraydah 51452, Saudi Arabia

* **Correspondence:** Email: maselim@uqu.edu.sa; Tel: +966537930306.

Abstract: The primary goal of this study is to create a novel mathematical model based on the time-stepping boundary element method (BEM) scheme for solving three-dimensional coupled dynamic thermoelastic fracture issues in anisotropic functionally graded materials (FGMs). The crack tip opening displacement determines the dynamic stress intensity factor (SIF). The effects of anisotropy, graded parameters, and angle locations on the SIF were studied for three-dimensional coupled dynamic thermoelastic fracture situations. The results show that the novel method is exceptionally exact and efficient at assessing the fracture mechanics of fractured thermoelastic anisotropic FGMs. In addition, this paper provides a theoretical framework for analyzing a wide range of real engineering applications.

Nomenclature:

α	Thermal expansion coefficient	n_j	Outward unit normal vector components
α_i^p	Unknown coefficient	k	Thermal conductivity
$\beta(\boldsymbol{x})$	Stress-temperature modulus	q	Heat flux
Γ	Boundary	q^*	Known heat flux

$\Delta\tau$	Time step	Q	Heat sources
μ	Shear modulus	r	$= \|x - x'\|$
$\tilde{\mu}$	Normalized shear modulus	$\mathbb{R}$	$= \|x - x^p\|$
ρ	Mass density	t_i	Tractions
σ_{ij}	Stress tensor	t_i^*	Known tractions
τ	Time	T	Temperature
$\varphi(R)$	Radial basis function (RBF)	$\tilde{T}$	Normalized temperature
$\phi^p(R)$	Fourth-order spline RBF	T^*	Known temperature
Ω	Domain	T_0	Initial temperature
a_i^k	Unknown coefficient	$\dot{T}$	Temperature time derivative
c_{ij} & c	Free-term coefficients	$\{T\}$	Nodal temperatures
c_p	Specific heat	u_i	Displacement vector
$C_{ijkl}(x)$	Elastic moduli	$\tilde{u}_i$	Normalized displacement
c_{ijkl}^{tip}	Crack-tip elastic moduli	u_i^*	Known displacements
d_p	Support domain size at x^p	$\boldsymbol{u}_0$	Initial displacement
E	Constant Young's modulus	$\dot{u}_{i,i}$	Volume strain rate
E'	FGM Young's modulus	$\ddot{u}_i$	Acceleration
F_i	Body force vector	$\{u\}$	Nodal displacements
k	Thermal conductivity	v	Poisson's ratio
$\tilde{k}$	Normalized thermal conductivity	$\boldsymbol{v}_0$	Initial velocity
m	Functionally graded parameter	$\boldsymbol{x}$	Field point
N_b	Boundary nodes number	$\boldsymbol{x}'$	Source point
N_i	Internal nodes number	x_s	Cartesian coordinate system
N_t	$= N_b + N_i$ total nodes number	$\boldsymbol{x}^p$	Application point

1. Introduction

Functionally graded materials (FGMs) are advanced composite materials whose composition and properties gradually change across the material, usually transitioning between two or more distinct phases, such as metal and ceramic. Unlike standard homogeneous materials, FGMs provide specialized qualities that can be optimized for specific purposes, such as increased strength, thermal resistance, or wear resistance, by altering the material gradient [1,2]. This continual variation in characteristics enables FGMs to endure complicated situations such as high-temperature gradients or mechanical pressures, making them excellent for use in aerospace, automotive, and biomedical engineering. FGMs provide considerable advantages over traditional materials by regulating the spatial distribution of material phases, particularly in applications that require both mechanical and thermal performance [3,4].

Anisotropic materials have qualities that vary depending on the direction in which they are measured, indicating that their behavior changes with different orientations, such as crystals or fiber-reinforced composites. Orthotropic materials, on the other hand, are a subset of anisotropic materials with three mutually perpendicular planes of symmetry, implying that their properties are directionally dependent but in a more defined and simpler manner—commonly seen in materials such as wood or

certain composites. Isotropic materials, on the other hand, have homogeneous properties in all directions, implying that their mechanical and thermal responses are equal regardless of the direction in which they are tested, as in metals and some polymers.

Understanding the differences between different material classes is important in material selection and structural design, especially when determining how a material will react to stress, strain, or heat in various applications. Understanding a material's anisotropy is also important for designing structures that can withstand complex, directed pressures in fields like aerospace, civil engineering, and materials research [5,6].

Fracture modes I, II, and III in anisotropic FGMs describe different types of fracture propagation behaviors under varied loading situations, with each mode determined by the FGMs' unique features, which change spatially. Mode I, also known as the opening mode, involves crack faces moving apart in a direction normal to the crack plane due to tensile stresses. In anisotropic FGMs, this mode is influenced by the directional dependence of material properties such as stiffness and Poisson's ratio, which can result in non-uniform crack tip stress fields [7–9]. Mode II, also known as the sliding mode, occurs when the crack faces slide past each other in a shear direction parallel to the crack plane [10,11]. In FGMs, the spatial gradient in material properties, particularly the shear modulus, affects the crack's resistance to sliding, depending on the material's variation across the crack front. Mode III, the tearing or anti-plane shear mode, is distinguished by crack faces moving in a shear direction perpendicular to the crack plane, with out-of-plane shear stresses; in anisotropic FGMs, the varying properties in the out-of-plane direction produce different shear resistances that influence the tearing behavior [12,13]. Because FGMs have both anisotropy (directional dependency) and inhomogeneity (gradients in material properties), cracks usually encounter a combination of all three modes, making fracture behavior more complex than in isotropic materials [14,15]. In such materials, the stress intensity factors (SIFs) for each mode must account for these spatial variations, and the crack tip fields are significantly altered by the heterogeneous nature of the material, resulting in intricate crack propagation dynamics influenced by both material gradients and directional dependencies [16,17].

Thermoelastic fracture problems in anisotropic FGMs involve the study of crack propagation and fracture behavior in materials that experience both thermal and mechanical loading, with material properties varying spatially and directionally. These materials exhibit gradients in thermal conductivity, elasticity, and other properties, which makes their response to stress and temperature changes more complex than homogeneous materials. When subjected to thermal gradients, the anisotropic nature of the FGM results in uneven thermal expansion or contraction, inducing internal stresses that interact with mechanical loading, influencing crack growth and fracture behavior. Analyzing these problems requires considering the coupled effects of thermal and mechanical stresses, with crack-tip stress intensity factors (SIFs) and energy release rates often varying due to the spatially varying material properties. Understanding these coupled effects is critical for designing reliable components in high-performance applications like aerospace, turbine engines, and biomedical devices, where FGMs are subjected to extreme thermal and mechanical conditions [18,19].

The boundary element method (BEM) is a powerful numerical method for resolving thermoelastic fracture issues in anisotropic FGMs, where material parameters like thermal conductivity, elasticity, and stiffness vary continuously across the structure. BEM is especially well-suited for these problems because it reduces the problem's dimensionality by converting the governing partial differential equations into integral equations defined only on the domain's boundary, which is useful when dealing with FGMs' complex, spatially varying properties. In thermoelastic fracture problems, BEM can

account for the combined effects of thermal and mechanical loads because temperature gradients provide extra stresses that interact with the material's directional dependence [20,21]. The material's anisotropy complicates the fracture analysis since stress intensity factors (SIFs) and energy release rates are affected by both the gradient and the material's directional characteristics. By discretizing the boundary and calculating the resulting integral equations, BEM can accurately predict crack propagation, stress distribution, and fracture behavior under combined thermal and mechanical loads. This makes BEM an effective tool for evaluating fracture mechanics in FGMs, especially in high-performance engineering applications like aerospace, where such materials are subjected to both heat gradients and mechanical pressures at the same time [22,23].

The radial integration boundary element method (RIBEM) and the radial integration finite element method (RIFEM) are two numerical techniques that use radial integration to solve boundary value problems, although they differ greatly in their formulation, application, and computing benefits. RIBEM, being a boundary-only approach, concentrates on discretizing the problem's border and solving only the boundary integral equations, resulting in lower computational cost and complexity as compared to standard domain-based methods such as the finite element method (FEM). It is especially useful for issues with infinite or semi-infinite domains, such as acoustics or electromagnetic field problems, where it is difficult to simulate the interior. RIFEM, on the other hand, incorporates radial functions into the finite element framework, handling both the domain and the boundary with radial basis functions (RBFs) and allowing for the modeling of complicated structures that consider both the interior and outside. While RIFEM allows for greater freedom in modeling inner fields and complicated geometries, it is computationally more expensive since it needs discretization of both the domain and the boundary, resulting in bigger system matrices and higher solution costs. Furthermore, because it focuses primarily on boundary discretization, RIBEM is generally easier to apply than RIFEM, which, while more versatile, may struggle with issues such as ill-conditioning in the system of equations or difficulties in capturing boundary effects near singularities. Both methods, however, seek to give high accuracy and efficiency in situations with irregular geometries, and the decision between them is mostly determined by the domain size, complexity, and available computer resources [24,25].

This work presents a time-stepping boundary element method for solving the 3D thermoelastic fracture problems of anisotropic FGMs. The crack tip opening displacement determines the dynamic SIF. Numerical findings demonstrate the current technique's accuracy and efficacy.

2. Formulation of the problem

In the current study, the graded material property has the following exponential function model [26]

$$E'(\mathrm{x}_s) = E e^{m\mathrm{x}_s} \quad (s = 1,2,3). \tag{1}$$

The governing equations are [25]

$$\sigma_{ij,j}(\mathrm{x},\tau) + b_i = \rho \ddot{u}_i(\mathrm{x},\tau), \tag{2}$$

$$\bar{T}(\mathrm{x},\tau) - \rho c_p \dot{T}(\mathrm{x},\tau) - \beta(\mathrm{x}) T_0 \dot{u}_{i,i}(\mathrm{x},\tau) = 0 \tag{3}$$

where $\overline{T}(\mathrm{x}, \tau) = (k(\mathrm{x})T_{,i}(\mathrm{x}, \tau))_{,i} + \psi(\mathrm{x}, \tau)$

Subjected to:

$$T(\mathrm{x}, \tau_0) \quad = T_0(\mathrm{x}), \tag{4}$$

$$u(\mathrm{x}, \tau_0) \quad = u_0(\mathrm{x}), \tag{5}$$

$$\dot{u}(\mathrm{x}, \tau_0) \quad = v_0(\mathrm{x}), \qquad \mathrm{x} \in \Omega \tag{6}$$

$$u_i(\mathrm{x}, \tau) = u_i^*(\mathrm{x}, \tau), \qquad \mathrm{x} \in \Gamma_u \tag{7}$$

$$t_i(\mathrm{x}, \tau) = \sigma_{ij}(\mathrm{x}, \tau)n_j = t_i^*(\mathrm{x}, \tau), \mathrm{x} \in \Gamma_t, \qquad \Gamma = \Gamma_u \cup \Gamma_t \tag{8}$$

$$T(\mathrm{x}, \tau) = T^*(\mathrm{x}, \tau), x \in \Gamma_T \tag{9}$$

$$q(\mathrm{x}, \tau) = -k \frac{\partial T(\mathrm{x}, \tau)}{\partial n} = q^*(\mathrm{x}, \tau), x \in \Gamma_q, \qquad \Gamma = \Gamma_T \cup \Gamma_q \tag{10}$$

where

$$\sigma_{ij}(\mathrm{x}, \tau) = C_{ijkl}(\mathrm{x})u_{k,l}(\mathrm{x}, \tau) - \delta_{ij}\beta(\mathrm{x})T(\mathrm{x}, \tau). \tag{11}$$

In which $t_i(\mathrm{x}, \tau) = \sigma_{ij}(\mathrm{x}, \tau)n_j$, $q(\mathrm{x}, \tau) = -k \frac{\partial T(\mathrm{x}, \tau)}{\partial n}$ and $\beta(\mathrm{x}) = \frac{E(\mathrm{x})}{1-2v}\alpha$.

3.   Radial integration boundary element method (RIBEM) implementation

The governing Eqs (2) and (3) can be written as [25]

$$\int_\Omega u_{ij}^*(\sigma_{jk,k} + b_j - \rho \ddot{u}_j) \mathrm{d}\Omega = 0, \tag{12}$$

$$\int_\Omega T^* \left[(kT_{,i})_{,i} + \psi - \rho c_p \dot{T} - \beta T_0 \dot{u}_{i,i} \right] \mathrm{d}\Omega = 0. \tag{13}$$

Thus, displacement and temperature integral equations are:

$$\int_\Gamma u_{ij}^* \sigma_{jk} n_k \, \mathrm{d}\Gamma - \int_\Gamma u_{ij,k}^* C_{ijkl} n_s u_r \, \mathrm{d}\Gamma + \int_\Omega u_{ij,ks}^* C_{ijkl} u_r \, \mathrm{d}\Omega + \int_\Omega u_{ij,k}^* C_{ijkl} u_r \, \mathrm{d}\Omega$$

$$+ \int_\Omega u_{ij,j}^* \beta T \, \mathrm{d}\Omega + \int_\Omega u_{ij}^* b_j \, \mathrm{d}\Omega - \int_\Omega u_{ij}^* \rho \ddot{u}_j \, \mathrm{d}\Omega = 0. \tag{14}$$

$$\int_\Gamma T^* kT_{,i} n_i \, \mathrm{d}\Gamma - \int_\Gamma kT T_{,i}^* n_i \, \mathrm{d}\Gamma + \int_\Omega kT T_{,ii}^* \, \mathrm{d}\Omega + \int_\Omega T^* \psi \mathrm{d}\Omega + \int_\Omega k_{,i} T_{,i}^* T \, \mathrm{d}\Omega$$

$$- \int_\Omega T^* \rho c_p \dot{T} \, \mathrm{d}\Omega - \int_\Omega T^* \beta T_0 \dot{u}_{i,i} \, \mathrm{d}\Omega = 0. \tag{15}$$

According to [27,28], the third terms of equations (10) and (11) are

$$\int_{\Omega} u_{ij,ks}^*(\mathbf{x}',\mathbf{x})C_{ijkl}(\mathbf{x}')u_r(\mathbf{x}',\tau)\mathrm{d}\Omega = -C_{ijkl}(\mathbf{x})u_i(\mathbf{x},\tau). \tag{16}$$

$$\int_{\Omega} kT\frac{\partial}{\partial x_i}\left(\frac{\partial T^*(\mathbf{x}',\mathbf{x})}{\partial x_i}\right)\mathrm{d}\Omega = -kT(\mathbf{x}',\tau). \tag{17}$$

Therefore, Eqs (10) and (11) yield

$$c_{ij}(\mathbf{x}')\tilde{u}_j(\mathbf{x}',\tau) = \int_{\Gamma} u_{ij}^*(\mathbf{x},\mathbf{x}')t_j(\mathbf{x},\tau)\mathrm{d}\Gamma - \int_{\Gamma} t_{ij}^*(\mathbf{x},\mathbf{x}')\tilde{u}_j(\mathbf{x},\tau)\mathrm{d}\Gamma + \int_{\Omega} u_{ij}^*(\mathbf{x},\mathbf{x}')b_j\,\mathrm{d}\Omega$$

$$+\int_{\Omega} W_{ij}(\mathbf{x},\mathbf{x}')\tilde{u}_j(\mathbf{x},\tau)\mathrm{d}\Omega - \int_{\Omega} u_{ij}^*(\mathbf{x},\mathbf{x}')\frac{\rho}{C_{ijkl}(\mathbf{x})}\ddot{u}_j(\mathbf{x},\tau)\mathrm{d}\Omega \tag{18}$$

$$+\int_{\Omega} u_{ij,j}^*(\mathbf{x},\mathbf{x}')\frac{\beta(\mathbf{x})}{k(\mathbf{x})}\tilde{T}(\mathbf{x},\tau)\mathrm{d}\Omega,$$

$$c(\mathbf{x}')\tilde{T}(\mathbf{x}',\tau) = \bar{\bar{T}}(\mathbf{x},\mathbf{x}') + \int_{\Omega} T^*(\mathbf{x},\mathbf{x}')\psi(\mathbf{x},\tau)\mathrm{d}\Omega$$

$$-\int_{\Omega} T^*(\mathbf{x},\mathbf{x}')\frac{\beta(\mathbf{x})T_0}{C_{ijkl}(\mathbf{x})}\dot{u}_{i,i}(\mathbf{x},\tau)\mathrm{d}\Omega. \tag{19}$$

where

$$\bar{\bar{T}}(\mathbf{x},\mathbf{x}') = -\int_{\Gamma} T^*(\mathbf{x},\mathbf{x}')q(\mathbf{x},\tau)\mathrm{d}\Gamma - \int_{\Gamma} \tilde{T}(\mathbf{x},\tau)q^*(\mathbf{x},\mathbf{x}')\mathrm{d}\Gamma + \int_{\Omega} V(\mathbf{x},\mathbf{x}')\tilde{T}(\mathbf{x},\tau)\mathrm{d}\Omega - \int_{\Omega} T^*(\mathbf{x},\mathbf{x}')\frac{\rho c_p}{k(\mathbf{x})}\dot{T}(\mathbf{x},\tau)\mathrm{d}\Omega.$$

The fundamental solutions can be expressed as [29]

$$u_{ij}^* = \begin{cases} \dfrac{1}{8\pi G \mathbb{K}_1}\left[\mathbb{K}_3\delta_{ij}\ln\dfrac{1}{r} + r_{,i}r_{,j}\right] \text{ for } 2D, \\ \dfrac{1}{16\pi G \mathbb{K}_1 r}\left[\mathbb{K}_3\delta_{ij} + r_{,i}r_{,j}\right] \text{ for } 3D. \end{cases} \tag{20}$$

$$t_{ij}^* = \begin{cases} \dfrac{-1}{4\pi \mathbb{K}_1 r}\left\{\dfrac{\partial r}{\partial n}\left[\mathbb{K}_2\delta_{ij} + 2r_{,i}r_{,j}\right] + \mathbb{K}_2\left(n_i r_{,j} - n_j r_{,i}\right)\right\} \text{ for } 2D, \\ \dfrac{-1}{8\pi \mathbb{K}_1 r^2}\left\{\dfrac{\partial r}{\partial n}\left[\mathbb{K}_2\delta_{ij} + 3r_{,i}r_{,j}\right] + \mathbb{K}_2\left(n_i r_{,j} - n_j r_{,i}\right)\right\} \text{ for } 3D. \end{cases} \tag{21}$$

$$T^* = \begin{cases} \dfrac{1}{2\pi}\ln\dfrac{1}{r} & \text{ for } 2D, \\ \dfrac{1}{4\pi r} & \text{ for } 3D. \end{cases} \tag{22}$$

$$q^* = \begin{cases} \dfrac{k}{2\pi r}\dfrac{\partial r}{\partial n} & \text{ for } 2D, \\ \dfrac{k}{4\pi r^2}\dfrac{\partial r}{\partial n} & \text{ for } 3D. \end{cases} \tag{23}$$

and

$$u_{ij,j}^* = \begin{cases} \dfrac{-\mathbb{K}_2}{4\pi \mathbb{K}_1}\dfrac{r_{,i}}{r} & \text{ for } 2D, \\ \dfrac{-\mathbb{K}_2}{8\pi \mathbb{K}_1}\dfrac{r_{,i}}{r^2} & \text{ for } 3D. \end{cases} \tag{24}$$

$$W_{ij} = \begin{cases} \dfrac{-1}{4\pi \mathbb{K}_1 r}\left\{\tilde{\mu}_{,k} r_{,k}\left[\mathbb{K}_2 \delta_{ij} + \beta r_{,i} r_{,j}\right] + \mathbb{K}_2\left(\tilde{\mu}_{,i} r_{,j} - \tilde{\mu}_{,j} r_{,i}\right)\right\} & \text{for } 2D, \\[4mm] \dfrac{-1}{8\pi \mathbb{K}_1 r^2}\left\{\tilde{\mu}_{,k} r_{,k}\left[\mathbb{K}_2 \delta_{ij} + \beta r_{,i} r_{,j}\right] + \mathbb{K}_2\left(\tilde{\mu}_{,i} r_{,j} - \tilde{\mu}_{,j} r_{,i}\right)\right\} & \text{for } 3D. \end{cases} \tag{25}$$

$$V = \frac{\partial \tilde{k}}{\partial \mathrm{x}_i}\frac{\partial T^*}{\partial \mathrm{x}_i}. \tag{26}$$

where

$$\tilde{u}_i = C_{ijkl} u_i, \qquad \tilde{\mu} = \ln C_{ijkl}, \qquad \tilde{T} = kT, \qquad \tilde{k} = \ln k, \quad \mathbb{K}_1 = 1 - v, \qquad \mathbb{K}_2 = 1 - 2v,$$
$$\mathbb{K}_3 = 3 - 4v. \tag{27}$$

A meshfree method is produced by using the RIM to convert the several domain integrals that arise in Eqs (18) and (19) into boundary integrals for evaluation. The unknown function u in RIM can be roughly determined using the following equations

$$u(\mathbf{x}) = \sum_p \alpha_i^p \varphi^p(R) + a_i^k \mathrm{x}_k + a_i^0 = \boldsymbol{\varphi}^T(\mathbf{x})\boldsymbol{\alpha}. \tag{28}$$

$$\sum_p \alpha_i^p = 0. \tag{29}$$

$$\sum_p \alpha_i^p \mathrm{x}_j^p = 0. \tag{30}$$

In this investigation, the following radial basis function is used

$$\phi^p(\mathbb{R}) = \begin{cases} 1 - 6\left(\dfrac{\mathbb{R}}{d_p}\right)^2 + 8\left(\dfrac{\mathbb{R}}{d_p}\right)^3 - 3\left(\dfrac{\mathbb{R}}{d_p}\right)^4 & 0 \leq \mathbb{R} \leq d_p \\ 0 & d_p \leq \mathbb{R}. \end{cases} \tag{31}$$

To generate the following algebraic equations system in matrix form, collocate x in Eq (28) at all points of application and combine it with Eqs (29) and (30):

$$\{u\} = [\phi]\{\alpha\}. \tag{32}$$

where

$$u(\mathbf{x}) = \boldsymbol{\varphi}^T(\mathbf{x})[\phi]^{-1}\{u\} = \Phi(\mathbf{x})\{u\}. \tag{33}$$

In which $\{\alpha\} = [\phi]^{-1}\{u\}$ and $\Phi(\mathbf{x}) = \boldsymbol{\varphi}^T(\mathbf{x})[\phi]^{-1}$.

The following boundary integral equations are obtained by inserting Eq (33) into Eqs (18) and (19) and then applying RIM

$$c_{ij}(\mathbf{x}')\tilde{u}_j(\mathbf{x}',\tau) = \int_\Gamma u_{ij}^*(\mathbf{x},\mathbf{x}')t_j(\mathbf{x},\tau)\mathrm{d}\Gamma - \int_\Gamma t_{ij}^*(\mathbf{x},\mathbf{x}')\tilde{u}_j(\mathbf{x},\tau)\mathrm{d}\Gamma$$

$$+ \int_\Gamma \frac{1}{r^\alpha(Q,p)}\frac{\partial r}{\partial \boldsymbol{n}}F_i^1(\mathbf{x},\mathbf{x}')\mathrm{d}\Gamma + \tilde{u}_j^k(\mathbf{x},\tau)\int_\Gamma \frac{1}{r^\alpha(\mathbf{x},\mathbf{x}')}\frac{\partial r}{\partial \boldsymbol{n}}F_{ijk}^2(\mathbf{x},\mathbf{x}')\mathrm{d}\Gamma \tag{34}$$

$$- \ddot{u}_j^k(\mathbf{x},\tau)\int_\Gamma \frac{1}{r^\alpha(Q,p)}\frac{\partial r}{\partial \boldsymbol{n}}F_{ijk}^3(\mathbf{x},\mathbf{x}')\mathrm{d}\Gamma + \tilde{T}^k(\mathbf{x},\tau)\int_\Gamma \frac{1}{r^\alpha(\mathbf{x},\mathbf{x}')}\frac{\partial r}{\partial \boldsymbol{n}}F_{ik}^4(\mathbf{x},\mathbf{x}')\mathrm{d}\Gamma,$$

and

$$c(\mathbf{x}')\tilde{T}(\mathbf{x}',\tau) = -\int_\Gamma T^*(\mathbf{x},\mathbf{x}')q(\mathbf{x},\tau)d\Gamma - \int_\Gamma q^*(\mathbf{x},\mathbf{x}')\tilde{T}(\mathbf{x},\tau)d\Gamma$$

$$+\int_\Gamma \frac{1}{r^\alpha(\mathbf{x},\mathbf{x}')}\frac{\partial r}{\partial \boldsymbol{n}}F^5(\mathbf{x},\mathbf{x}')d\Gamma + \tilde{T}^k(\mathbf{x},\tau)\int_\Gamma \frac{1}{r^\alpha(\mathbf{x},\mathbf{x}')}\frac{\partial r}{\partial \boldsymbol{n}}F_k^6(\mathbf{x},\mathbf{x}')d\Gamma \tag{35}$$

$$-\dot{\tilde{T}}^k(\mathbf{x},\tau)\int_\Gamma \frac{1}{r^\alpha(\mathbf{x},\mathbf{x}')}\frac{\partial r}{\partial \boldsymbol{n}}F_k^7(\mathbf{x},\mathbf{x}')d\Gamma - \tilde{u}_{i,i}^\beta(\mathbf{x},\tau)\int_\Gamma \frac{1}{r^\alpha(\mathbf{x},\mathbf{x}')}\frac{\partial r}{\partial \boldsymbol{n}}F_k^8(\mathbf{x},\mathbf{x}')d\Gamma,$$

in which

$$F_i^1(\mathbf{x},\mathbf{x}') = \int_0^{r(x,x\prime)} u_{ij}^*(\mathbf{x},\mathbf{x}')r_1(\mathbf{x},\mathbf{x}')dr(\mathbf{x}), \tag{36}$$

$$F_{ijk}^2(\mathbf{x},\mathbf{x}') = \int_0^{r(x,x\prime)} W_{ij}(\mathbf{x},\mathbf{x}')r_2(\mathbf{x},\mathbf{x}')dr(\mathbf{x}), \tag{37}$$

$$F_{ijk}^3(\mathbf{x},\mathbf{x}') = \int_0^{r(\mathbf{x},x^p)} u_{ij}^*(\mathbf{x},\mathbf{x}')\frac{\rho c_p}{k(q)}r_2(\mathbf{x},\mathbf{x}')dr(\mathbf{x}), \tag{38}$$

$$F_{ik}^4(\mathbf{x},\mathbf{x}') = \int_0^{r(\mathbf{x},x^p)} u_{ij,j}^*(\mathbf{x},\mathbf{x}')\frac{\beta(\mathbf{x})}{k(\mathbf{x})}r_2(\mathbf{x},\mathbf{x}')dr(\mathbf{x}), \tag{39}$$

$$F^5(\mathbf{x},\mathbf{x}') = \int_0^{r(\mathbf{x},x^p)} T^*(\mathbf{x},\mathbf{x}')r_3(\mathbf{x},\mathbf{x}')dr(\mathbf{x}), \tag{40}$$

$$F_k^6(\mathbf{x},\mathbf{x}') = \int_0^{r(\mathbf{x},x^p)} V(\mathbf{x},\mathbf{x}')r_2(\mathbf{x},\mathbf{x}')dr(\mathbf{x}), \tag{41}$$

$$F_k^7(\mathbf{x},\mathbf{x}') = \int_0^{r(\mathbf{x},x^p)} T^*(\mathbf{x},\mathbf{x}')\frac{\rho c_p}{k(\mathbf{x})}r_2(\mathbf{x},\mathbf{x}')dr(\mathbf{x}), \tag{42}$$

$$F_k^8(\mathbf{x},\mathbf{x}') = \int_0^{r(\mathbf{x},x^p)} T^*(\mathbf{x},\mathbf{x}')\frac{\beta(\mathbf{x})T_0}{\mu(\mathbf{x})}r_2(\mathbf{x},\mathbf{x}')dr(\mathbf{x}). \tag{43}$$

where $r_1(\mathbf{x},\mathbf{x}') = b_j r^\alpha(\mathbf{x},\mathbf{x}'), r_2(\mathbf{x},\mathbf{x}') = \Phi_k(\mathbf{x})r^a(\mathbf{x},\mathbf{x}'), r_3(\mathbf{x},\mathbf{x}') = \psi(\mathbf{x},t)r^\alpha(\mathbf{x},\mathbf{x}')$.

The radial integrals in Eqs (36)–(43) are evaluated using the following relations:

$$x_i = x_i' + r_i r, \quad \mathbb{R} = \sqrt{r^2 + 2sr + \overline{\mathbb{R}}^2}, \quad s = r_i\overline{\mathbb{R}}_i, \quad \overline{\mathbb{R}}_i = x_i' - x_i^A. \tag{44}$$

The boundary Γ discretization and numerical integration of Eqs (34) and (35) produce

$$M\ddot{\tilde{u}} + H_u\tilde{u} - W\tilde{u} - G_u t - A\tilde{T} = F_u, \tag{45}$$

$$C\dot{\tilde{T}} + H_T\tilde{T} - V\tilde{T} - G_T q + B\dot{\tilde{u}} = F_T. \tag{46}$$

By putting the boundary conditions into Eqs (45) and (46), we obtain [25]

$$M\ddot{\tilde{u}} + \overline{W}x - A\tilde{T} = \overline{F}^1, \tag{47}$$

$$C\dot{\tilde{T}} + \overline{V}y + B\dot{\tilde{u}} = \overline{F}^2. \tag{48}$$

If we assumed that $x = \begin{Bmatrix} t_{n_t} \\ \tilde{u}_{n_u} \end{Bmatrix}$ and $y = \begin{Bmatrix} q_{n_q} \\ \tilde{T}_{n_T} \end{Bmatrix}$, Eqs (47) and (48) can be represented as

$$\begin{cases} \boldsymbol{M}_{12}\ddot{\tilde{\boldsymbol{u}}}_{n_u} + \overline{\boldsymbol{W}}_{11}t_{n_t} + \overline{\boldsymbol{W}}_{12}\tilde{\boldsymbol{u}}_{n_u} - \mathbb{A}_{11}\tilde{\boldsymbol{T}}_{n_q} - \mathbb{A}_{12}\tilde{\boldsymbol{T}}_{n_T} = \overline{\boldsymbol{F}}^1_{n_t} \\ \boldsymbol{M}_{22}\ddot{\tilde{\boldsymbol{u}}}_{n_u} + \overline{\boldsymbol{W}}_{21}t_{n_t} + \overline{\boldsymbol{W}}_{22}\tilde{\boldsymbol{u}}_{n_u} - \mathbb{A}_{21}\tilde{\boldsymbol{T}}_{n_q} - \mathbb{A}_{22}\tilde{\boldsymbol{T}}_{n_T} = \overline{\boldsymbol{F}}^1_{n_u} \end{cases}, \tag{49}$$

$$\begin{cases} \boldsymbol{C}_{11}\dot{\tilde{\boldsymbol{T}}}_{n_q} + \boldsymbol{C}_{12}\dot{\tilde{\boldsymbol{T}}}_{n_T} + \overline{\mathbb{V}}_{11}\boldsymbol{q}_{n_q} + \overline{\mathbb{V}}_{12}\tilde{\boldsymbol{T}}_{n_T} + \boldsymbol{B}_{12}\dot{\tilde{\boldsymbol{u}}}_{n_u} = \overline{\boldsymbol{F}}^2_{n_q} \\ \boldsymbol{C}_{21}\dot{\boldsymbol{T}}_{n_q} + \boldsymbol{C}_{22}\dot{\boldsymbol{T}}_{n_T} + \overline{\mathbb{V}}_{21}\boldsymbol{q}_{n_q} + \overline{\mathbb{V}}_{22}\tilde{\boldsymbol{T}}_{n_T} + \boldsymbol{B}_{22}\dot{\tilde{\boldsymbol{u}}}_{n_u} = \overline{\boldsymbol{F}}^2_{n_T} \end{cases}. \tag{50}$$

Substituting vector t_{n_t} into Eq (49) yields Eq (51) below. Similarly, substituting vector $\boldsymbol{q}_{n_q}$ into Eq (50) yields Eq (52) below

$$\tilde{M}\ddot{\tilde{u}} + \tilde{W}\tilde{u} - \tilde{\mathbb{A}}\tilde{T} = \bar{F}_1, \tag{51}$$

$$\tilde{C}\dot{\tilde{T}} + \tilde{\mathbb{V}}\tilde{T} + \tilde{B}\dot{\tilde{u}} = \bar{F}_2. \tag{52}$$

where matrices $\boldsymbol{M}$ and W are $3N_t \times 3N_t$, $\mathbb{A}$ is $3N_t \times N_t$ as well as $\boldsymbol{C}$ and $\mathbb{V}$ are $N_t \times N_t$, and $\boldsymbol{B}$ is $N_t \times 3N_t$.

In which total nodes $N_s = N_b$ boundary nodes $+ N_i$ internal nodes.

Adding Eqs (51) and (52) results in the following unified system:

$$\overline{M}\ddot{X} + \overline{C}\dot{X} + \overline{K}X = \overline{F}. \tag{53}$$

The Houbolt time-integration technique has various advantages, notably when handling dynamic problems in structural analysis. One of the primary advantages is its simplicity and ease of implementation. The Houbolt methodology, being an explicit method, is simple to employ, particularly for problems requiring high computational efficiency. It also uses less memory than more complex implicit methods because it only needs the current and prior time-step values to calculate. Furthermore, Hublot's approach can manage large time steps in some cases, making it useful for issues in which high-frequency oscillations or tiny time-step requirements are not crucial. The method is stable for situations with moderate damping and, because it is conditionally stable, it performs well when a suitable time step size is chosen, reducing the need for unnecessarily small steps. Furthermore, Houbolt's technique is frequently utilized in explicit dynamic analyses, particularly structural dynamics, and vibration analysis, because it delivers fast answers at minimal processing costs, making it useful for real-time simulations or large-scale issues. However, it should be noted that its accuracy can diminish when dealing with stiff systems or when higher-order accuracy is required, making it better suited to non-stiff or moderately stiff systems.

To solve Eq (53), we use the Houbolt technique with the assumption that acceleration varies linearly throughout the time interval $(t, t + \Delta t)$. Therefore, we have

$$\ddot{X}_{t+\Delta t} = \frac{2X_{t+\Delta t} - 5X_t + 4X_{t-\Delta t} - X_{t-2\Delta t}}{\Delta t^2}, \tag{54}$$

$$\dot{X}_{t+\Delta t} = \frac{11X_{t+\Delta t} - 18X_t + 9X_{t-\Delta t} - 2X_{t-2\Delta t}}{6\Delta t}. \tag{55}$$

To determine the unknowns $X_{t+\Delta t}$ for every time-step, substitute Eqs (54) and (55) into Eq (53) and solve the following algebraic equation

$$\left(\overline{K} + \frac{2}{\Delta t^2}\overline{M} + \frac{11}{6\Delta t}\overline{C}\right)X_{t+\Delta t} = \left(\frac{5}{\Delta t^2}\overline{M} + \frac{3}{\Delta t}\overline{C}\right)X_t - \left(\frac{4}{\Delta t^2}\overline{M} + \frac{3}{2\Delta t}\overline{C}\right)X_{t-\Delta t} \tag{56}$$

$$+ \left(\frac{1}{\Delta t^2}\overline{M} + \frac{1}{3\Delta t}\overline{C}\right)X_{t-2\Delta t} + \overline{F}_{t+\Delta t}.$$

First, Eq (56) is solved to yield displacements and temperatures for each time step. Differentiating Eq (33) with respect to x yields the nodal strains at every given time step. The associated stresses are then calculated with Eq (11).

According to [30], the crack tip stress in FGMs is

$$\sigma_{ij}(r,\theta) = \frac{K_{\mathrm{I}}}{\sqrt{2\pi r}}\bar{\sigma}_{ij}^{\mathrm{I}}(\theta) + \frac{K_{\mathrm{II}}}{\sqrt{2\pi r}}\bar{\sigma}_{ij}^{\mathrm{II}}(\theta) + \frac{K_{\mathrm{III}}}{\sqrt{2\pi r}}\bar{\sigma}_{ij}^{\mathrm{III}}(\theta), \tag{57}$$

and the crack tip displacements in FGMs can be expressed as

$$u_i(r,\theta) = \frac{1}{c_{ijkl}^{tip}}\sqrt{\frac{r}{2\pi}}\left[K_{\mathrm{I}}\bar{u}_i^{\mathrm{I}}(\theta) + K_{II}\bar{u}_i^{\mathrm{II}}(\theta) + K_{\mathrm{III}}\bar{u}_i^{\mathrm{III}}(\theta)\right]. \tag{58}$$

where (r,θ) are the polar coordinates, and $\bar{u}_i^I, \bar{u}_i^{\mathrm{II}}, \bar{u}_i^{\mathrm{III}}, \bar{\sigma}_{ij}^I(\theta), \bar{\sigma}_{ij}^{\mathrm{II}}(\theta)$, and $\bar{\sigma}_{ij}^{\mathrm{III}}(\theta)$ are the same as that of the homogeneous one.

Therefore, the SIFs for the cracked thermoelastic anisotropic FGMs are [30]

$$K_{\mathrm{I}} = \lim_{r \to 0}\left(\frac{2c_{ijkl}^{tip}}{\kappa+1}\sqrt{\frac{\pi}{2r}}\Delta u_2\right), \tag{59}$$

$$K_{\mathrm{II}} = \lim_{r \to 0}\left(\frac{2c_{ijkl}^{tip}}{\kappa+1}\sqrt{\frac{\pi}{2r}}\Delta u_1\right), \tag{60}$$

$$K_{\mathrm{III}} = \lim_{r \to 0}\left(\frac{c_{ijkl}^{tip}}{2}\sqrt{\frac{\pi}{2r}}\Delta u_3\right). \tag{61}$$

To solve coupled dynamic thermoelastic fracture issues in anisotropic FGMs, computing the crack tip displacements $\Delta u_i(t)$ and substituting them into the Eqs (59)–(61) may obtain the dynamic SIFs for the cracked thermoelastic anisotropic FGMs. Thus, the current paper provides a theoretical framework for analyzing a wide range of real engineering applications.

4. Numerical results and discussion

There is no closed-form analytical solution for the nonhomogeneous materials mentioned here, i.e., FGMs, because finding an analytical solution to the problem is extremely challenging. The proposed BEM created in this work is suitable for a broad range of dynamic thermoelastic fracture problems in anisotropic FGMs.

To exhibit the numerical results derived using the proposed technique specified in this paper, the elasticity tensor, temperature coefficient, and thermal conductivity for homogeneous and functionally graded materials, respectively, are [31]:

$$C_{pjkl} = \begin{bmatrix} 430.1 & 130.4 & 18.2 & 0 & 0 & 201.3 \\ 130.4 & 116.7 & 21.0 & 0 & 0 & 70.1 \\ 18.2 & 21.0 & 73.6 & 0 & 0 & 2.4 \\ 0 & 0 & 0 & 19.8 & -8.0 & 0 \\ 0 & 0 & 0 & -8.0 & 29.1 & 0 \\ 201.3 & 70.1 & 2.4 & 0 & 0 & 147.3 \end{bmatrix} \text{GPa}$$

$$\beta_{pj} = \begin{bmatrix} 1.01 & 2.00 & 0 \\ 2.00 & 1.48 & 0 \\ 0 & 0 & 7.52 \end{bmatrix} \cdot 10^6 \, N/Km^2$$

$$k_{pj} = \begin{bmatrix} 5.2 & 0 & 0 \\ 0 & 7.6 & 0 \\ 0 & 0 & 38.3 \end{bmatrix} W/Km$$

$$k_{pj} = \begin{bmatrix} 5.2 & 0 & 0 \\ 0 & 7.6 & 0 \\ 0 & 0 & 38.3 \end{bmatrix} \left(3 + \cos^2\left(\frac{x}{2} + \frac{y}{3}\right) \right) W/Km$$

Example 1. An anisotropic FGM plate with cracks

Figure 1 shows an anisotropic FGM plate with two parallel cracks, with the following parameters: $T_0 = 100°C$, $l = 24$ cm, $a = 2$ cm, $b = 3$ cm. The plate's border is meshed by 60 boundary elements, with 15 boundary elements meshing each crack.
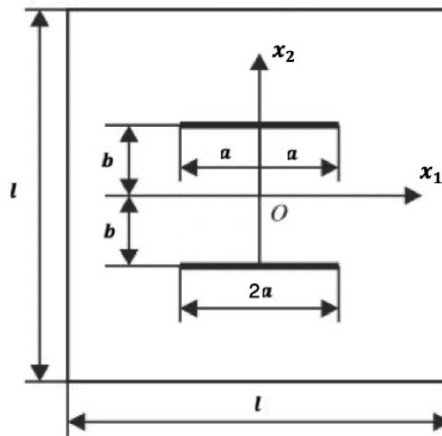

Figure 1. An anisotropic FGM plate with two parallel cracks.

Figure 2 demonstrates that in the functionally graded case, the stress intensity component rises to its highest value, whereas in the homogenous case, it falls to its lowest. Isotropic materials in the $0 \leq t \leq 0.8$ range have smaller sizes and greater stress intensity factor values compared to other functionally graded materials in the $0.8 < t$ range. In the homogeneous instance, the isotropic case is smaller than other materials in the range of $0 < t < 4$.

Figure 3 illustrates how the SIF of two crack tips varies over time for different thermoelastic coupling parameter values ($\beta = 0.0, 0.3, 0.6$), where $\beta = 0.0$ represents the uncoupled thermoelastic scenario. The graph indicates that increasing the thermoelastic coupling parameter lowers the SIF.
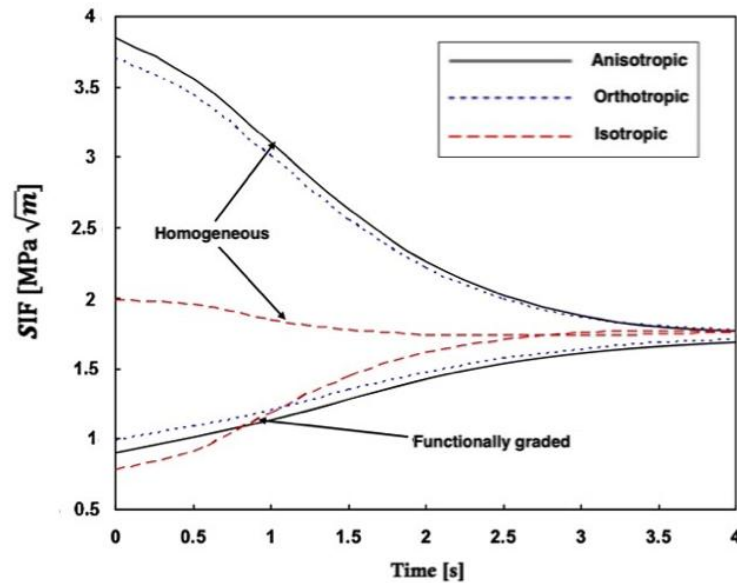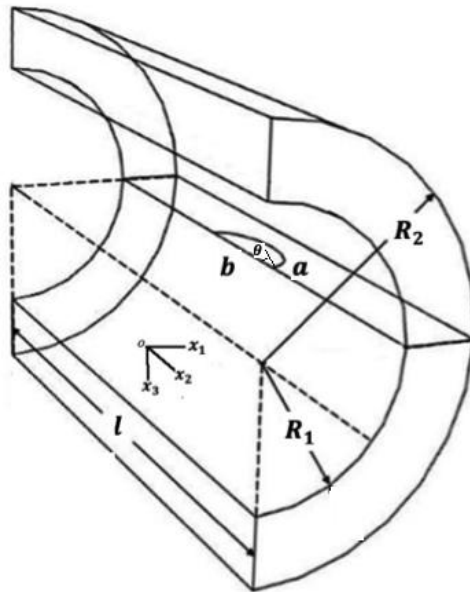
Figure 2. The variation of the SIF over time for different materials in homogeneous and functionally graded cases.
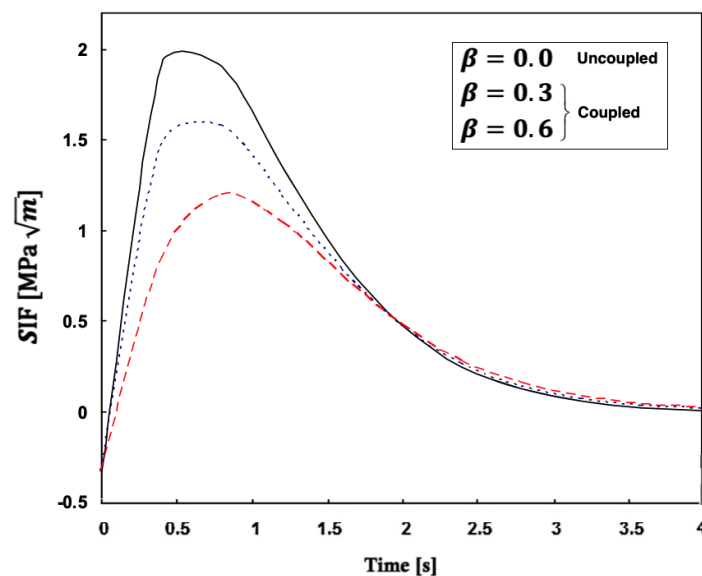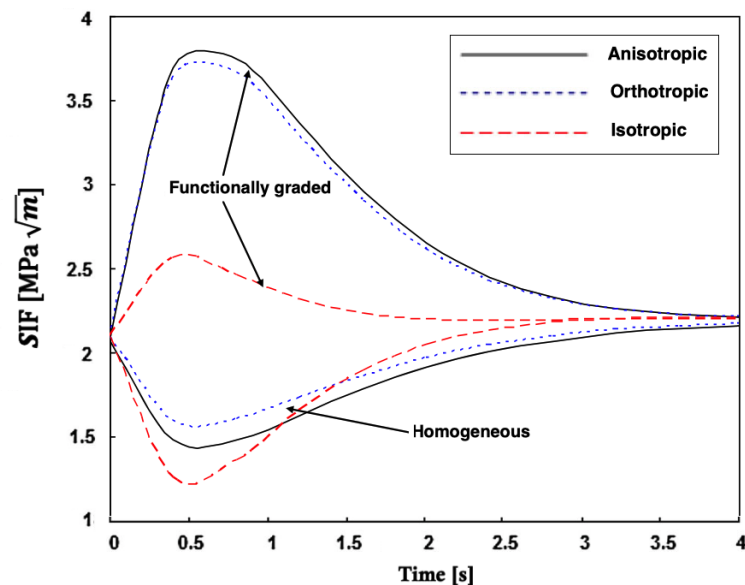

Figure 3. Variation of the SIF with time for different coupling parameter values.

Example 2. 3D anisotropic FGM circular thick tube with an elliptical crack

Figure 4 shows a 3D anisotropic FGM circular thick tube with an elliptical crack, with the following properties: tube length $l = 35$ cm, tube inner radius $R_1 = 10$ cm, tube outer radius $R_2 = 15$ cm, initial temperature $T_0 = 100°C$, $a = 4$ cm, and $b = 2$ cm. To tackle this issue, the model is discretized into 360 border elements and 120 internal nodes.

Figure 4. Considered circular tube model.

Figure 5. Variation of the SIF over time for different materials in homogeneous and functionally graded cases.

Figure 5 shows that in the functionally graded case, anisotropic materials have higher SIFs compared to other materials. However, in the homogeneous case, isotropic materials have lower SIFs compared to other materials in the $0 \leq t \leq 1.15$ and higher SIFs compared to other materials in the $1.15 < t$ range until reaching a maximum value.
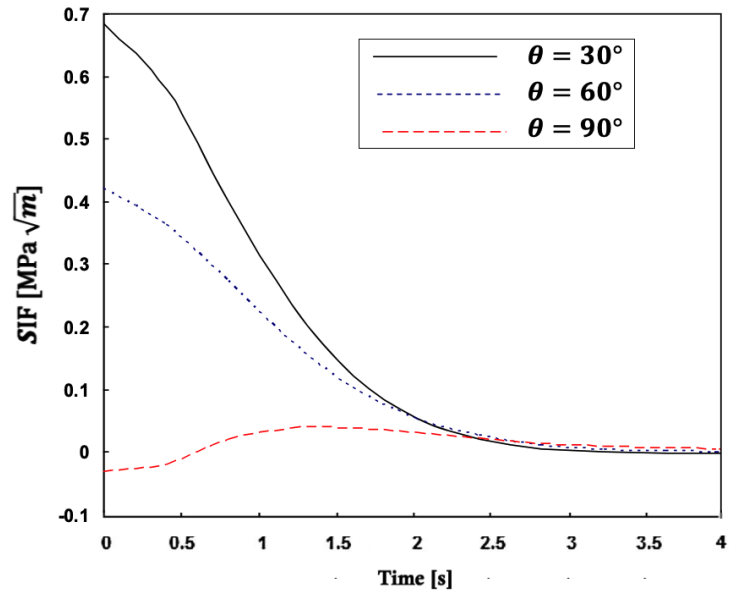
Figure 6. Variation of the SIF with time for different angle points along the crack front.

Figure 6 depicts how the SIF varies over time for three different angle positions ($\theta = 30°, 60°, 90°$) along the crack front. This figure shows that raising the angle decreases the SIF.
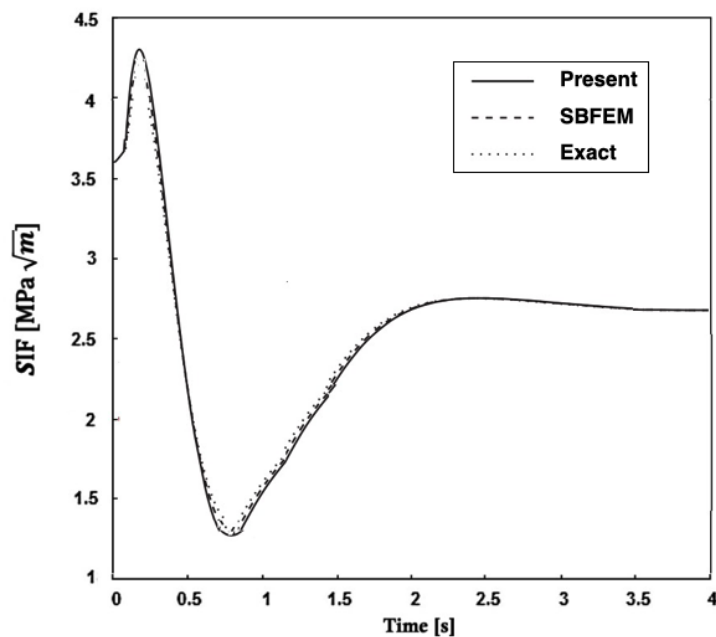
Figure 7. Variation of the SIF with time for BEM, SBFEM, and S-XMM-N.

There are no previously published results to substantiate the proposed technique's findings. Some literature can be included in the proposed inquiry. As a result, in our study, we analyzed a one-dimensional specific situation and compared our RIBEM (present) results to Iqbal et al.'s scaled

boundary finite element method (SBFEM) results [32] and Pan's exact solution results [33].

Figure 7 depicts the variations of SIF with time for current BEM, SBFEM [32], and Exact [33]. These results reveal that the current BEM has great agreement with the SBFEM and Exact, demonstrating the accuracy and correctness of our proposed technique.

5. Conclusions

The primary goal of this study is to establish a time-stepping boundary element technique (BEM) for solving three-dimensional coupled dynamic thermoelastic fracture issues in anisotropic functionally graded materials (FGMs). The crack tip opening displacement determines the dynamic stress intensity factor (SIF). The effects of anisotropy, graded parameters, and angle locations on the SIF are studied for three-dimensional coupled dynamic thermoelastic fracture situations. Results show that the novel method is exceptionally exact and efficient at assessing the fracture mechanics of fractured thermoelastic anisotropic FGMs. Because FGMs are nonhomogeneous materials, the crack modes are constantly heterogeneous and difficult; yet the examples show that the developed coupled thermoelastic RIBEM is well suited for studying the dynamic fracture problems of FGMs in both 2D and 3D. The modeling processes are basic and can yield accurate results.

Author contributions

Mohamed Abdelsabour Fahmy: Conceptualization, Methodology, Software, Validation, Formal Analysis, Investigation, Resources, Data curation, Writing—original draft, Writing—review & editing; Ahmad Almutlg:Formal: Analysis, Investigation, Resources, Data curation, Writing—original draft, Writing—review & editing. All authors have read and agreed to the published version of the manuscript.

Use of Generative-AI tools declaration

The authors declare they have not used Artificial Intelligence (AI) tools in the creation of this article.

Acknowledgments

Funding

Conflicts of Interest

The authors declare no conflict of interest.

References

1. S. Zghal, F. Dammak, Functionally Graded Materials: Analysis and Applications to FGM, FG-CNTRC and FG Porous Structures, Boca Raton, Florida: CRC press, 2024. https://doi.org/10.1201/9781003483786

2. S. Zghal, D. Ataoui, F. Dammak, Free vibration analysis of porous beams with gradually varying mechanical properties. Proceedings of the Institution of Mechanical Engineers, *P. I. Mech. Eng. M.-J. Eng.*, **236** (2022), 800–812. https://doi.org/10.1177/14750902211047746

3. S. Trabelsi, S. Zghal, F. Dammak, Thermo-elastic buckling and post-buckling analysis of functionally graded thin plate and shell structures, *J. Braz. Soc. Mech. Sci. Eng.*, **42** (2020), 233. https://doi.org/10.1007/s40430-020-02314-5

4. N. Joueid, S. Zghal, M. Chrigui, F. Dammak, Thermoelastic buckling analysis of plates and shells of temperature and porosity dependent functionally graded materials, *Mech. Time-Depend. Mater.*, **28** (2024), 817–859. https://doi.org/10.1007/s11043-023-09644-6

5. M. A. Fahmy, M. Toujani, A New Fractional Boundary Element Model for the 3D Thermal Stress Wave Propagation Problems in Anisotropic Materials, *Math. Comput.Appl.*, **30** (2025), 6. https://doi.org/10.3390/mca30010006

6. M. A. Fahmy, Three-dimensional boundary element sensitivity analysis of anisotropic thermoelastic materials, *J. Umm Al-Qura Univ. Appl. Sci.*, (2025). https://doi.org/10.1007/s43994-024-00210-5

7. F. Delale, F. Erdogan, The crack problem for a nonhomogeneous plane, *J. Appl. Mech.*, **50** (1983), 609–614. https://doi.org/10.1115/1.3167098

8. L. C. Guo, N. Noda, Modeling method for a crack problem of functionally graded materials with arbitrary properties piecewise-exponential model, *Int. J. Solids Struct.*, **44** (2007), 6768–6790. https://doi.org/10.1016/j.ijsolstr.2007.03.012

9. F. Erdogan, B. H. Wu, Crack problems in FGM layers under thermal stresses, *J. Therm. Stresses*, **19** (1996), 237–265. https://doi.org/10.1080/01495739608946172

10. N. Noda, Z. H. Jin, Thermal stresses intensity factors for a crack in a strip of a functionally graded material, *Int. J. Solids Struct.*, **30** (1993), 1039–1056. https://doi.org/10.1016/0020-7683(93)90002-O

11. N. Noda, Z. H. Jin, Thermal stresses around a crack in the nonhomogeneous interfacial layer between two dissimilar elastic half-planes, *Int. J. Solids Struct.*, **41** (2004), 923–945. https://doi.org/10.1016/j.ijsolstr.2003.09.056

12. Z. H. Jin, N. Noda, Crack-tip singular fields in non-homogeneous body with crack in thermal stress fields, *J. Appl. Mech.*, **61** (1994), 738–740. https://doi.org/10.1115/1.2901529

13. N. Noda, Thermal stresses intensity for functionally graded plate with an edge crack, *J. Therm. Stresses*, **20** (1996), 373–387. https://doi.org/10.1080/01495739708956108

14. K. H. Lee, Analysis of a propagating crack tip in orthotropic functionally graded materials, *Compos. Part B: Eng.*, **84** (2016), 83–97. https://doi.org/10.1016/j.compositesb.2015.08.068

15. Y. D. Lee, F. Erdogan, Interface Cracking of FGM Coating under Steady State Heat Flow, *Eng. Fract. Mech.*, **59** (1998), 361–380. https://doi.org/10.1016/S0013-7944(97)00137-9

16. P. Gu, M. Dao, R. J. Asrao, A Simplified Method for Calculating the Crack-tip Field of Functionally Graded Materials Using the Domain Integral, *J. Appl. Mech.*, **66** (1999), 101–108. https://doi.org/10.1115/1.2789135

17. B. N. Rao, S. Rahman, Meshfree analysis of cracks in isotropic functionally graded materials, *Eng. Fract. Mech.*, **70** (2003), 1–27. https://doi.org/10.1016/S0013-7944(02)00038-3

18. M. A. Fahmy, A Three-Dimensional CQBEM Model for Thermal Stress Sensitivities in Anisotropic Materials, *Appl. Math. Inf. Sci.* **19** (2025), 489–495. http://dx.doi.org/10.18576/amis/190301

19. M. A. Fahmy, Three-dimensional Boundary Element Modeling for The Effect of Rotation on the Thermal Stresses of Anisotropic Materials, *Appl. Math. Inf. Sci.*, **19** (2025), 379–386. http://dx.doi.org/10.18576/amis/190213

20. M. A. Fahmy, BEM Modeling for Stress Sensitivity of Nonlocal Thermo-Elasto-Plastic Damage Problems, *Computation*, **12** (2024), 87. https://doi.org/10.3390/computation12050087

21. M. A. Fahmy, M. Toujani, Fractional Boundary Element Solution for Nonlinear Nonlocal Thermoelastic Problems of Anisotropic Fibrous Polymer Nanomaterials, *Computation*, **12** (2024), 117. https://doi.org/10.3390/computation12060117

22. M. A. Fahmy, A new boundary element model for magneto-thermo-elastic stress sensitivities in anisotropic functionally graded materials, *J. Umm Al-Qura Univ. Eng. Archit.*, 2025. https://doi.org/10.1007/s43995-025-00100-9

23. M. A. Fahmy, A time-stepping DRBEM for nonlinear fractional sub-diffusion bio-heat ultrasonic wave propagation problems during electromagnetic radiation, *J Umm Al-Qura Univ Appl Sci*, 2024. https://doi.org/10.1007/s43994-024-00178-2

24. M. A. Fahmy, R. A. A. Jeli, A New Fractional Boundary Element Model for Anomalous Thermal Stress Effects on Cement-Based Materials, *Fractal Fract.*, **8** (2024), 753. https://doi.org/10.3390/fractalfract8120753

25. B. Zheng, Y. Yang, X. Gao, C. Zhang, Dynamic fracture analysis of functionally graded materials under thermal shock loading by using the radial integration boundary element method, *Compos. Struct.*, **201** (2018), 468–476. https://doi.org/10.1016/j.compstruct.2018.06.050

26. H. A. Atmane, A. Tounsi, S. A. Meftah, H. A. Belhadj, Free vibration behavior of exponential functionally graded beams with varying cross-section, *J. Vib. Control*, **17** (2011), 311–318. https://doi.org/10.1177/1077546310370691

27. K. Yang, X. W. Gao, Radial integration BEM for transient heat conduction problems, *Eng. Anal. Bound. Elem.*, **34** (2010), 557–563.

28. X. W. Gao, C. Zhang, J. Sladek, V. Sladek, Fracture analysis of functionally graded materials by a BEM, *Compos. Sci. Technol.*, **68** (2008), 1209–1215. https://doi.org/10.1016/j.compscitech.2007.08.029

29. X. W. Gao, Boundary element analysis in thermoelasticity with and without internal cells, *Int. J. Numer. Methods Eng.*, **57** (2003), 957–990. https://doi.org/10.1002/nme.715

30. F. Erdogan, Fracture mechanics of functionally graded materials, *Int. J. Solids Struct.*, **5** (1995), 753–770. https://doi.org/10.1016/0961-9526(95)00029-M

31. P. N. J. Rasolofosaon, B. E. Zinszner, Comparison between permeability anisotropy and elasticity anisotropy of reservoir rocks, *Geophysics*, **67** (2002), 230–240. https://doi.org/10.1190/1.1451647

32. M. D. Iqbal, C. Birk, E.T. Ooi, S. Natarajan, H. Gravenkamp, Transient thermoelastic fracture analysis of functionally graded materials using the scaled boundary finite element method, *Theor. Appl. Fract. Mec.*, **127** (2023), 104056. https://doi.org/10.1016/j.tafmec.2023.104056

33. E. Pan, Exact Solution for Functionally Graded Anisotropic Elastic Composite Laminates, *J. Compos. Mater.*, **37** (2003), 1903–1920. https://doi.org/10.1177/002199803035565